



Facile microwave assisted synthesis of N-rich carbon quantum dots/dual-phase TiO₂ heterostructured nanocomposites with high activity in CO₂ photoreduction

Mengli Li^{a,*}, Min Wang^b, Longfeng Zhu^a, Yiming Li^a, Zheng Yan^a, Zhongquan Shen^a, Xuebo Cao^{a,*}

^a School of Biology and Chemical Engineering, Jiaxing University, Jiaxing, Zhejiang 314001, PR China

^b State Key Laboratory of High Performance Ceramics and Superfine Microstructure, Shanghai Institute of Ceramics, Chinese Academy of Sciences, 1295 Ding-Xi Road, Shanghai 200050, PR China

ARTICLE INFO

Keywords:

Nanocomposite
CO₂ Photoreduction
Carbon quantum dots
TiO₂

ABSTRACT

In this work, several efficient heterostructured nanocomposites with enhanced CO₂ photoreduction activity were successfully constructed by anchoring carbon quantum dots onto TiO₂ using a facile microwave assisted synthesis strategy. The carbon quantum dots obtained by microwave treatment of thiourea and citric acid acted as a sensitizer in the composites to enhance light absorption. The high-resolution transmission electron microscopy (HR-TEM) revealed that a closely integrated interface between carbon quantum dots and TiO₂ nanosheets was formed in the heterostructured nanocomposites. Furthermore, the photogenerated charge transfer and separation in the heterogeneous nanocomposites were demonstrated to be significantly improved when compared with that in pristine TiO₂. Consequently, a remarkable enhancement of photocatalytic activity evaluated for CO₂ photoreduction under simulated solar light irradiation can be found in the nanocomposites. Maximum CH₄ and CO yields of 0.769 and 1.153 μmol, respectively, have been obtained from the photoreduction after one hour irradiation without any noble metal loaded on photocatalyst. The amounts of CH₄ and CO generated over nanocomposite are 7.79 and 7.61 times as high as those on pristine TiO₂. This encouraging performance in CO₂ photoreduction shows that these nanocomposites might be a prospective material in environmental protection and energy conversion.

1. Introduction

In recent years, energy shortage and global warming resulted from the combustion of fossil fuels have attracted a great deal of public concerns, since it would probably bring about severe energy, environmental and even economic problems [1,2]. Among various potential solutions, solar-energy-driven conversion of CO₂ into hydrocarbon and/or other carbon based chemicals with higher energy is probably one of the best ways, since it can simultaneously generate chemical fuels to meet energy demand and mitigate environmental problems. On a long term basis, the utilization of inexhaustible and clean solar power resource is an essential component of solutions to address growing energy demand in the whole world [3]. Since the first scientific report of artificial photosynthesis, which is featured with CO₂ conversion into organic substances with H₂O as both electron donor and proton source under sunlight irradiation, reported by Fujishima and his coworkers in 1979 [4], a growing interest in the development of photocatalysts that are capable of solar sensitivity and capture of CO₂ has been evolved [5].

Among various photocatalysts, TiO₂ remains to be one of the most commonly used semiconductors owing to its outstanding physical and chemical capability, such as excellent photochemical stability, superior biocompatibility, relatively high surface area, low-cost, and efficient charge transfer and separation [6–9]. Up to now, TiO₂ based nanomaterials have been widely used in dye-sensitized solar cells, water splitting, gas sensors, pollutants degradation and artificial photosynthesis [10–13]. However, due to its intrinsic wide band gap (about 3.2 eV), it is only photoactive under ultraviolet (UV) light irradiation which contributes around 4% of solar energy. Therefore, TiO₂ photocatalysts have a great limit on their energy harvest efficiency [14]. For different kinds of TiO₂, P25 consisted of mixed phase (80% of the anatase phase and 20% of the rutile phase of TiO₂) is a well-known and widely used commercial material because of its outstanding photoactivity and stability. In order to enhance the solar-to-fuel conversion efficiency, photocatalysts are required to have appropriate light absorption ability as well as fast and enhanced photo-generated charge transfer and separation efficiency [15]. Recently, a number of methods

* Corresponding authors.

E-mail addresses: menglil@mail.zjxu.edu.cn (M. Li), [xbiao@mail.zjxu.edu.cn](mailto:xbciao@mail.zjxu.edu.cn) (X. Cao).

have been exploited to meet these requirements, such as loading of novel metals (Pt [16], Au [17], Ag [18] and so on) co-catalysts onto the TiO₂ based semiconductor photocatalysts' surface, heteroatom (e.g. Co [19], N [20], S [21]) doping, and structure construction (e.g. 0D [8,22], 1D nanorod [23] and nanotube [17]). Among them, surface sensitization such as coupling TiO₂ with other visible-light-responsive materials could also enhance its visible light absorption ability [20,24]. Zhu et al. reported a cocatalyst hydridation approach for enhancing the photocatalytic conversion of CO₂ into CH₄ [25]. They found that the photocatalytic selectivity in CH₄ production could be significantly increased from 3.2% to 63.6% on Pd {100} and from 15.6% to 73.4% on Pd {111}. In addition, surface modification by La leads to the generation of oxygen vacancies and Ti³⁺, thus enhances the catalyst's activity in CO₂ photoreduction [8].

Carbon quantum dots (denoted as CQDs), which are known as a novel class of recently discovered carbon materials, have been garnered a lot of research attention because of their excellent photo induced electron transfer, electron reservoir properties and good up-converted photoluminescence behavior [10]. The emissions of such passivated CQDs covered a broad range of the visible region and extended into the near-infrared (NIR) region, which accounts for more than 50% of solar spectrum [26]. Besides, CQDs could not only be prepared inexpensively by facile methods and on a large scale, but also offer distinguished photophysical properties without incurring toxicity or elemental scarcity [27]. Coupling CQDs with other semiconductor photocatalysts have opened a new way for fully utilizing the spectrum of sunlight. The CQDs in the nanocomposites played an important role in harvesting visible light and facilitating the excited electron transfer along interfaces, resulting enhanced charge separation and stabilization [10,28]. Furthermore, it is reported that light-weight heteroatom-doped (such as B, N, P, and S) carbonaceous materials showed enhanced electrical conductivity to accelerate the electron transport and enlarged specific surface area to increase the binding sites [29]. It is reported that the introduction of nitrogen and sulfur into sp²-hybridized carbon frameworks would modulate their electrical conductivity and chemical activity, which effectively results in excellent catalytic performance [29,30]. The remarkable properties of P25 and heteroatom-doped CQDs motivate us to consider that whether we can rationally design a new class of heteroatom-doped CQDs/P25 hybrid with much stronger and wider absorption properties for efficient photocatalysts. Although CQDs can be assembled on the surface of some UV or visible photocatalytic active nanoparticles to yield some photoactive materials, it is still a great challenge for the synthesis of such interesting heteroatom-doped CQDs/P25 hybrid with tunable CQDs loading amount for maximizing the photocatalytic performance by one-pot facile method.

Herein, we demonstrated one-pot facile microwave-assisted method for the in-situ synthesis of N, S-containing CQDs/P25 heterostructured nanocomposites with tunable CQDs loading amount for enhancing the photocatalytic reduction of CO₂ with H₂O as reductant and proton donor. In this heterostructured system, the CQDs served as the bridge for carrying and transferring electrons from the two-phased TiO₂. As is known to all, photoabsorption, charge transfer and separation are the three main factors influencing the photoactivities of semiconductors. Hence, the effect of CQDs on the surface of P25, diffuse reflectance spectroscopy, photocurrent density, the results from activity tests in CO₂ photoreduction reaction, and electrochemical impedance spectroscopy (EIS) analysis reveal that such photocatalysis enhancement of N, S co-doped CQDs/P25 can be ascribed to the superior light absorbance and charge separation efficiency induced by CQDs. To the best of our knowledge, this is the first report on N, S-containing CQDs/P25 nanocomposites for the reduction of CO₂ with H₂O.

2. Experimental section

2.1. Synthesis procedure

All the chemicals used in this work were of analytical reagent grade and used as received without further treatment. P25 (anatase 80%, rutile 20%, Degussa Co. Ltd., Germany), citric acid, thiourea, anhydrous ethanol, and acetone were purchased from Sinopharm. Deionized (DI) water was generated on site using a Millipore system. The other reactants including iodine and Na₂SO₄ were supplied by Sigma.

Preparation of N, S-containing carbon quantum dots (denoted as NCQDs): NCQDs were synthesized by a facile one-pot microwave-assisted method. In a typical experiment, a weighted quantity of (0.5 g) citric acid and (0.5 g) thiourea were dissolved in 30 ml deionized water. After being stirred for 1 h, 10 ml of the solution was transferred into 80 ml Teflon-lined vial. Subsequently, the vial was placed in a commercial microwave oven (Glantz, 800 w, 2.45 GHz) for 7 min. After cooling down to room temperature naturally, the dark brown product was subjected to dialysis for 24 h in order to obtain NCQDs. After the dialysis, the obtained NCQDs solution was finally diluted to a concentration of 10 mg mL⁻¹ for further experimentation.

Synthesis of NCQDs/P25 heterostructured nanocomposites: 0.5 g P25 and certain amount of NCQDs solution were dispersed in 30 mL deionized water under consecutively ultrasonic treatment for 30 min. Secondly, the mixture was heated at 80 °C for 12 h under vigorous stirring. Finally, the resulting samples were washed several times with deionized water and ethanol, lyophilized overnight, and denoted as x-P25, where x represents the dosage of NCQDs raw materials by gram in equal proportion.

2.2. Characterization

The crystal structure of these synthesized samples was analyzed by power X-ray diffraction patterns (XRD, Rigaku D/Max 2200PC, Japan) using Cu K α radiation ($\lambda = 1.5406 \text{ \AA}$). The scan range of 2θ was 10–80° at a scanning rate of 4°/min with X-ray tube operated at 40 mA and 40 kV at room temperature. Transmission electron microscopy (TEM) and high-resolution transmission electron microscopy (HRTEM) images of the samples were obtained by JEM-2100F field emission transmission electron microscope (FE-TEM) operated at 200 kV equipping with an energy-dispersive X-ray (EDX) instrument. X-ray Photoelectron Spectroscopy (XPS) was recorded on a Thermo Scientific ESCALAB 250 spectrometer equipped with an Al monochromatic X-ray source and multichannel detector. High-resolution FT-IR spectra were conducted on Nicolet Avatar 330 FT-IR spectrometer. All the binding energy values for the high resolution were calibrated at 284.6 eV with contaminated carbon C 1s as reference. Ultraviolet visible (UV-vis) reflectance spectra were recorded on a UV-3101 PC Shimadzu spectroscope with a diffuse reflectance accessory. The spectra were recorded in the range of 200–800 nm, and BaSO₄ was used as the reference sample (100% reflectance). Elemental analysis (C, N, S) was taken on Elementar Vario EL III microanalyzer. Photoluminescence (PL) spectra were recorded on a Hitachi F-4500 with an excitation wavelength of 325 nm at room temperature. Fluorescence lifetime spectra were also recorded at room temperature with a fluorescence spectrophotometer (Fluo Time 100), and the excitation wavelength was 350 nm. Finally, Brunauer-Emmett-Teller (BET) specific surface area of the samples was characterized by sorption using Micromeritics Tristar 2000 instrument at 77 K.

2.3. Photoelectrochemical measurements

Photoelectrochemical (PEC) properties of these samples were carried out on a CHI 660A electrochemical workstation (Shanghai Chenhua Instrument, Inc.) with a standard three-electrode cell, in which Fluorine-doped Tin Oxide (FTO) supported photocatalysts served

as a working electrode. While the reference electrodes and the counter were Ag/AgCl and a platinum wire respectively, with 0.2 M Na₂SO₄ as electrolyte solution. The working electrodes were prepared by electro-photoretic deposition in acetone solution containing 12 mg of the sample powder and 3 mg of iodine. Two parallel FTO glasses were kept in the solution for 10 min with a 10 V bias under potentiostat control. All the samples are deposited onto FTO glasses, and the coated area was fixed at 1 cm². After being calcined for 2 h in an oven at 450 °C, a homogeneous thin film can be obtained.

2.4. Photocatalytic activity evaluation

Phtotocatalytic activities of the samples were evaluated by CO₂ photocatalytic reduction and conversion in a gas-closed circulation system by using a reactor purchased from PerfectLight Company (China, Beijing) with the volume of 500 mL. The reactor is made of borosilicate glass, while its window at the top is composed of optical quartz. In order to remove possible trace organic contaminants, all the samples were treated at 200 °C for 3 h in air before being tested. In a typical process, 50 mg photocatalyst was uniformly dispersed on a flat glass plate with an area of 1.5 cm × 1.5 cm. The glass plate was fixed in the center of reactor. A 300 W of Xenon-arc lamp (Aulight CEL-HX, Beijing) with sunlike radiation spectrum was used as the light source and put on the top of quartz window with the distance of 10 cm. The temperature of the whole reactor was controlled at 25 °C by cooling water circulation. Prior to illumination, the reactor was first purged with high purity CO₂ (99.99%) gas, monitored by a mass flow controller, was led to pass through a water bubbler to generate a mixture of CO₂ and water vapor. After being stood for one hour, an adsorption-desorption balance in the reactor could be established. The Xe lamp was then turned on to start the experiment. The gas phase products were sampled from the glass chamber at a given time intervals (1 h) for detecting CH₄ and/or other carbon-based gases. CO can also be detected by installing a methanizer, using N₂ as carrier gas. The products were analyzed by a gas chromatograph (GC-2060, Fuli Corp., China) with a flame ionization detector (FID) equipped with a TDX-01 packed column and a 5A molecular column. The isotope-tracer experiment was also carried out to study the carbon source of these observed carbonaceous products, using ¹³CO₂ instead of ¹²CO₂, while other photocatalytic procedure and conditions like CO₂ pressure were the same. The products were analyzed by gas chromatography-mass spectrometry (7890A and 5975C, Agilent).

3. Results and discussion

3.1. Characterization of the as-prepared samples

The morphology of the synthesized samples were analyzed by the powder X-ray diffraction technique, as shown in Fig. 1. These patterns show contributions from anatase (JCPDS 21-1272) as well as rutile (JCPDS 21-1276) phases. According to Zhang's [31] calculation method, the weight fraction of rutile phase appeared in P25 (WR) is about 19.4%. In detail, the calculation is WR = AR/(0.884AA + AR), where AA and AR represent intensities of the strongest (101) peak of anatase and (110) peak of rutile, respectively. It seems that the NCQDs loading did not change the crystallographic phase of the TiO₂ supports, since unnoticeable changes in the patterns

can be found between TiO₂ supports and the heterostructured nanocomposites. All the diffraction peaks of the heterostructured nanocomposites have no shift compared with pure TiO₂, indicating that NCQDs were not incorporated into the lattice of TiO₂, but were well deposited on the surface [32]. No diffraction peaks derived from NCQDs in these nanocomposites can be detected, which are probably attributed to their high dispersion, low content and/or poor crystallinity.

The morphological nature of TiO₂, NCQDs and the nanocomposites

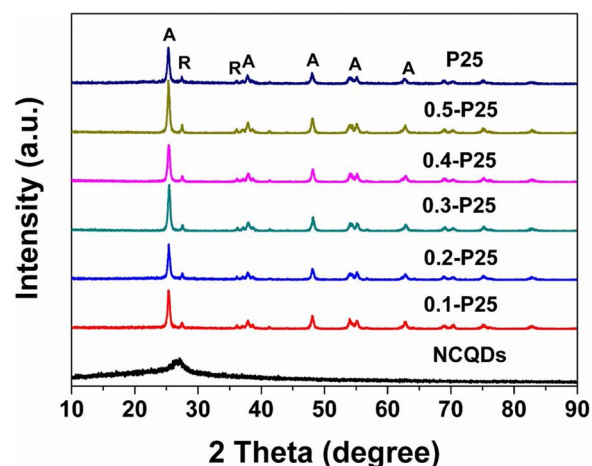


Fig. 1. XRD patterns of pristine P25, NCQDs and the heterostructured nanocomposites.

were analyzed by TEM and HR-TEM as depicted in Fig. 2. As can be seen in Fig. 2a, pure TiO₂ sample with even size are composed of nanosheets. Fig. 2b shows the TEM image of NCQDs obtained by fast microwave assisted method. After measuring 100 or so random carbon dots by TEM, we find that these as prepared carbon dots presented a quasi-spherical morphology with diameters ranging from 2.6 nm to 4.1 nm and their average diameter was 3.5 nm (particle distribution can be seen in Fig. S1a). Furthermore, high-resolution TEM image demonstrated the distinct (100) lattice planes with interfringe spacing of about 0.21 nm (Fig. S1b). The powder XRD patterns for NCQDs displayed an intense peak located at around 26° (Fig. S1c), which are in good agreement with the HR-TEM results, showing the crystalline graphitic carbon structure [33]. Although the broad peak may suggest the presence of amorphous NCQDs, there was no evidence for this type of carbon by HR-TEM. Therefore, the broadening of such diffraction peak might be related to these particles' nanometer size [34]. When assembled on the surface of TiO₂, the NCQDs retain the same morphology as shown in Fig. 2c and d. It is notable to find that the addition of NCQDs has only slight influence on TiO₂'s specific surface area and no impact of its pore size as shown in Table S1, which means that the NCQDs are on the surface of TiO₂ but not in its pores. The small black spots in white circle corresponding to NCQDs were well deposited on TiO₂ surface, which was also confirmed by TEM-EDX in Fig. S2. The chemical composition in both TiO₂ and the NCQDs/P25 was listed Table S2. Fig. 2d depicted the HR-TEM of NCQDs/TiO₂ heterostructured nanocomposites, and the white arrows pointed to NCQDs. The interplanar spacing of 0.345 nm corresponds to the (101) crystal planes of anatase of TiO₂ [35]. Other resolved interlayer distances were also identified for the (111) crystal plane of rutile (0.221 nm) and (101) plane of carbon (0.202 nm [34], as can be seen in Fig. S3) respectively, indicating the formation of the heterostructure [28], which is beneficial to photogenerated charge separation and electron transfer when compared with the pure TiO₂ sample.

Surface chemical compositions and valence states of various elements in the synthesized materials, and the interaction between GCQDs and TiO₂ were studied by X-ray photoelectron spectroscopy (XPS) as shown in Fig. 3. Specifically, high-resolution scanning XPS spectrum of C 1s mainly contains four asymmetrical peaks at 288.4, 286.0, 285.3, and 284.4 eV, which are attributed to C=O, C—OH, C—N, and C—C groups of the surface adventitious carbon, respectively. The intensity of C 1s in the nanocomposites became much lower when compared with that of pure NCQDs, while the banding energies have no obvious change (Fig. 3a). For the pure TiO₂ sample, the Ti 2p XPS spectra are identical with Ti 2p_{1/2} and Ti 2p_{3/2} peaks centered at binding energy values of 464.5 and 458.9 eV, respectively, which are consistent with the typical values for TiO₂ [36]. It is interesting to find that the binding

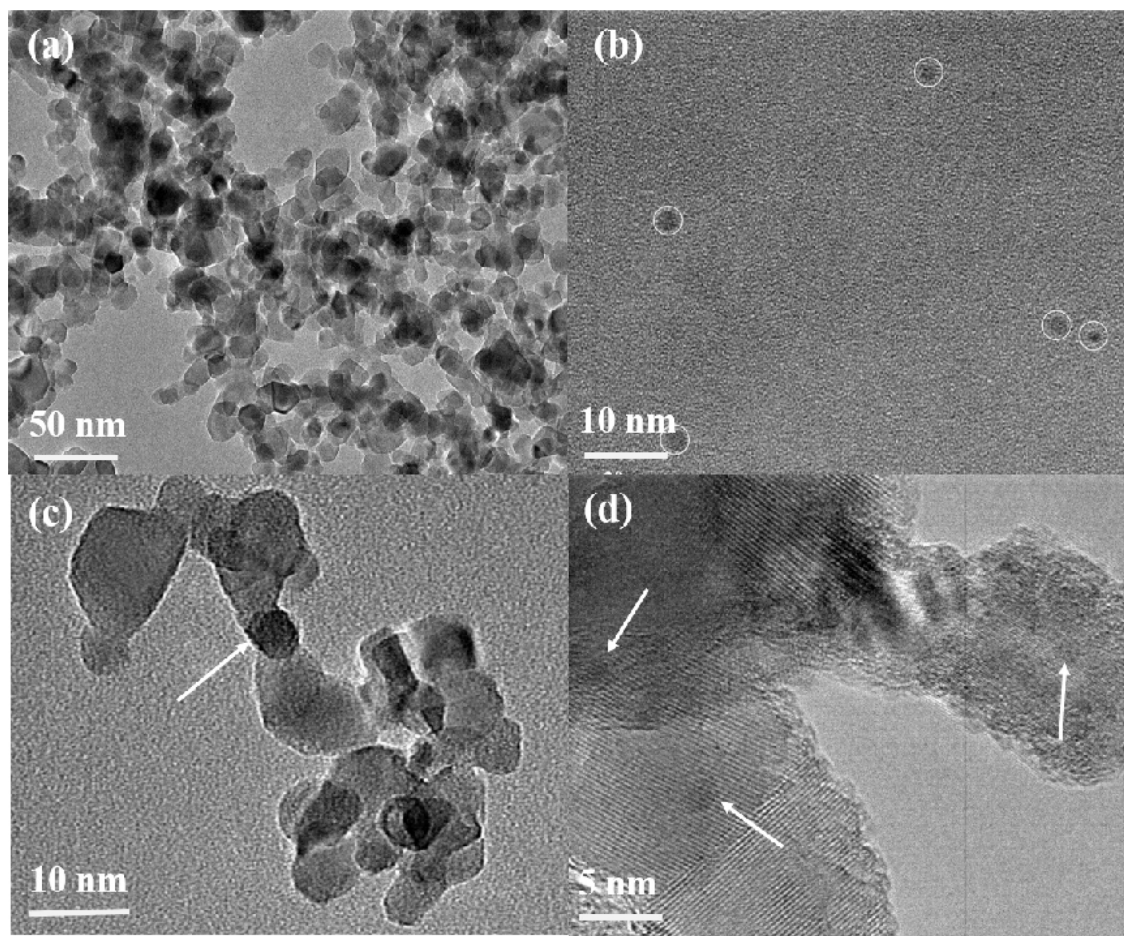


Fig. 2. Low-magnification TEM image of (a) P25; high-magnification TEM image of NCQDs (b); high-magnification TEM (c), and HR-TEM images of 0.4-P25 nanocomposite (d).

energy of Ti 2p in the nanocomposites shows positive shift (Fig. 3b), which can be seen as evidence of chemical bonding formation between NCQDs and TiO_2 [37]. Fig. 3c displays the spectrum of O 1s devided into two peaks at around 532.1 and 530.1 eV that can be assigned to O–H and Ti–O bonds, which are attributed to Ti–OH linkages and Ti–O–

Ti functional groups on the surface of the nanocomposites [38,39]. After being modified by NCQDs, the binding energy of O 1s in 0.4-P25 showed a negative shift, revealing chemical interaction emergence between the two components [40]. In addition to C, Ti and O peaks that are expected for carbon quantum dots and TiO_2 , nitrogen and sulfur

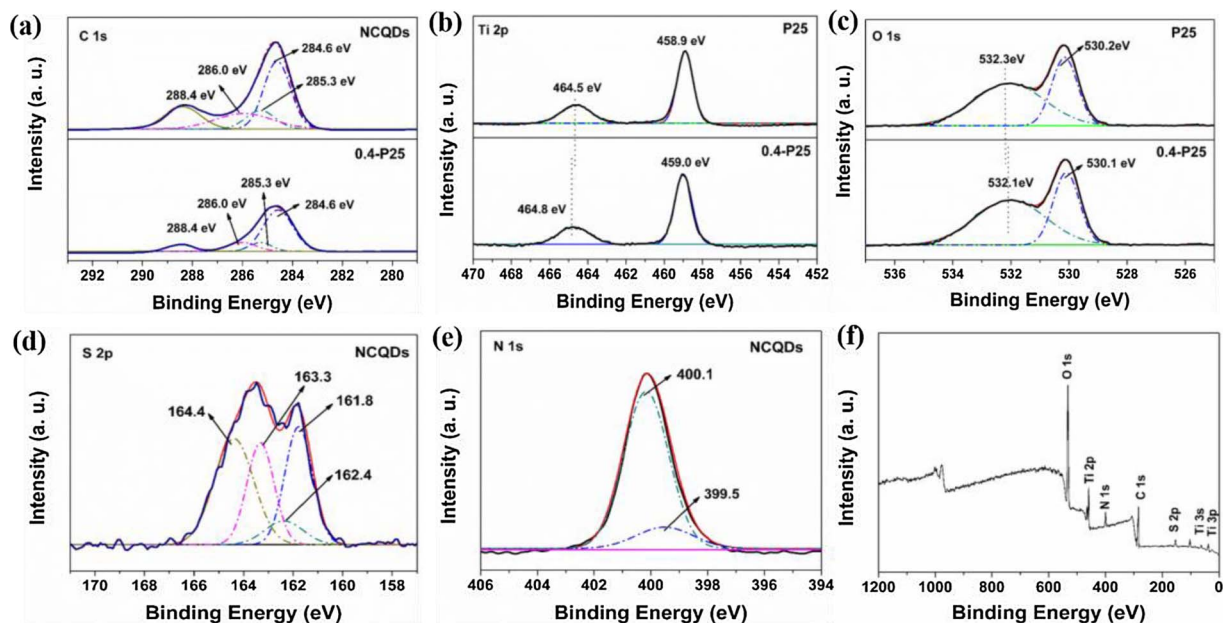


Fig. 3. (a) XPS profiles of C 1s (a), Ti 2p (b), O 1s (c), S 2p (d), N 1s (e), in NCQDs, and survey of 0.4-P25 nanocomposite (f).

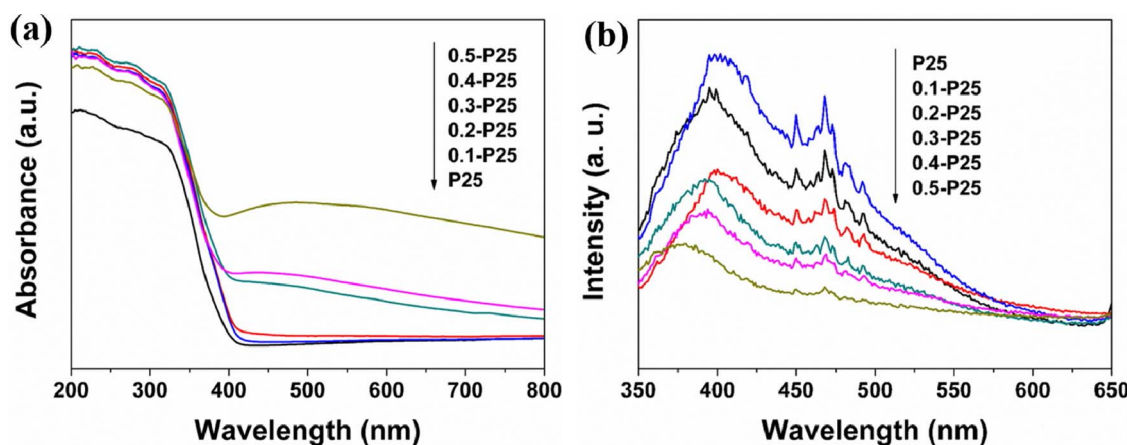


Fig. 4. (a) (UV-vis) diffuse reflectance spectra (DRS); (b) Photoluminescence spectra of the as-prepared samples excited at 325 nm.

signals were observed in NCQDs. The N 1s spectrum (Fig. 3e) demonstrates two peaks at 399.52 and 400.1 eV, which are identified as C–N–C and N–(C)₃ groups, respectively [29]. As shown in Fig. 3d, four peaks can be seen in S 2p spectrum, which are associated with the sulfoxide (164.4 eV), –C=S– (163.3 eV), C–Sn–C (162.4 eV, n = 1 or 2), and -SH (161.8 eV) groups, respectively [38]. The survey scan spectrum (Fig. 3f) indicates the presence of C, N, S, Ti and O in the sample. These results confirm the efficient functionalization of NCQDs with oxygen and sulfur containing groups. Moreover, FT-IR spectrum of NCQDs (Fig. S4) shows that multiple functionalities exist on the surface of NCQDs. The peak emerged at 3431 cm⁻¹ corresponds to the stretching mode of N–H and O–H [41], implying the good hydrophilicity of NCQDs. The peak centered at 3144 cm⁻¹ is assigned to the stretching vibration of C–H group. The band at 1705 cm⁻¹ is originated from the vibration absorption of C = O in COOH. Additionally, the peak 1185 cm⁻¹ comes from C=S vibration bonds [42].

(UV-vis) diffuse reflectance spectra (DRS) was employed to investigate the optical absorption properties of the synthesized samples in the range of 200–800 nm and the results are shown in Fig. 4. The strong absorption band at around 380 nm were ascribed to the intrinsic absorption of TiO₂, resulting from electron excitation of O 2p to Ti 3d [36]. As one can see from Fig. 4 a, pristine TiO₂, whose bandgap was around 3.2 eV, can only absorb light with wavelength shorter than 400 nm. However, after being modified by NCQDs, the samples showed much enhanced light absorption in both ultraviolet and visible light range. These results provide a direct evidence for the enhanced light absorption because of NCQDs photosensitization. The optical properties and element content including C, N and S of these synthesized heterostructured photocatalysts were also studied and listed in Table 1. The band gap energies (E_g) can be obtained according to Eq. (1):

$$E_g = h \frac{c}{\lambda} \quad (1)$$

where E_g is the band gap energy (eV), h the Planck's constant, c the light velocity (m/s) and λ is the absorption threshold wavelength (nm) [43,44]. CH₄ selectivity was calculated and listed in Table 1 based on electron transfer number, which is a little higher over most catalysts decorated by NCQDs and reaches its maximum of 0.61 on the sample 0.3-P25. This phenomenon is very interesting and deserves further study.

PL analysis was also performed to demonstrate that the NCQDs nanoparticles effectively accept excitons and prolong the lifetime of charge carriers on the photocatalyst surface during catalytic process. Fig. 4b shows PL spectra of P25 and the nanocomposites in wavelength range of 350–650 nm. The major emission peak at about 398 nm is assigned to TiO₂, whereas the other peak at around 468 nm can be attributed to band-edge free excitons. It is clear to see that the PL quench becomes more and more efficient with the addition of NCQDs, since the photogenerated electrons could transfer more easily in the nanocomposites. Effective charge carrier separation will definitely improve the lifetime of excited electrons and holes, and hence enhance the photocatalytic activity.

The excitation and transfer of photogenerated charge carriers in these samples were further investigated by photoelectrochemical (PEC) measurements. Fig. 5a shows photocurrent densities vs time curve in 0.1 M Na₂SO₄ aqueous solution with several 30 s light on/off cycles at 0.3 V. The prepared samples exhibited excellent stability after 420 s PEC test. Fast and uniform photocurrent response can be observed upon the light-on and light-off, which indicates the extremely fast charge transport in these as-prepared samples. A quickly increasing current emerges once the light is on and sharply declines when the light is off. This transient delay results from the electron trapping and releasing

Table 1
Physicochemical properties and element content of the photocatalysts for CO₂ reduction under full light irradiation.

Sample	λ_g (nm) ^a	Bandgap ^b (eV)	C (%) ^c	N (%)	S (%)	CH ₄ selectivity ^d	Lifetime ^e (ns)
NCQDs	–	–	46.59	15.75	2.015	–	–
0.1-P25	393	3.16	0.781	0.023	0.014	0.58	4.170
0.2-P25	400	3.10	0.804	0.019	0.040	0.58	4.174
0.3-P25	405	3.06	0.887	0.036	0.031	0.61	4.284
0.4-P25	414	2.99	0.947	0.197	0.022	0.54	4.327
0.5-P25	416	2.98	1.184	0.167	0.033	0.43	4.301
P25	418	2.97	–	–	–	0.52	4.165

^a Absorption threshold of the catalysts.

^b Calculated bandgap energies of the samples.

^c Element content by weight.

^d CH₄ selectivity were calculated based on electron transfer number involved in CO₂ photoreduction.

^e Average lifetime of the synthesized samples.

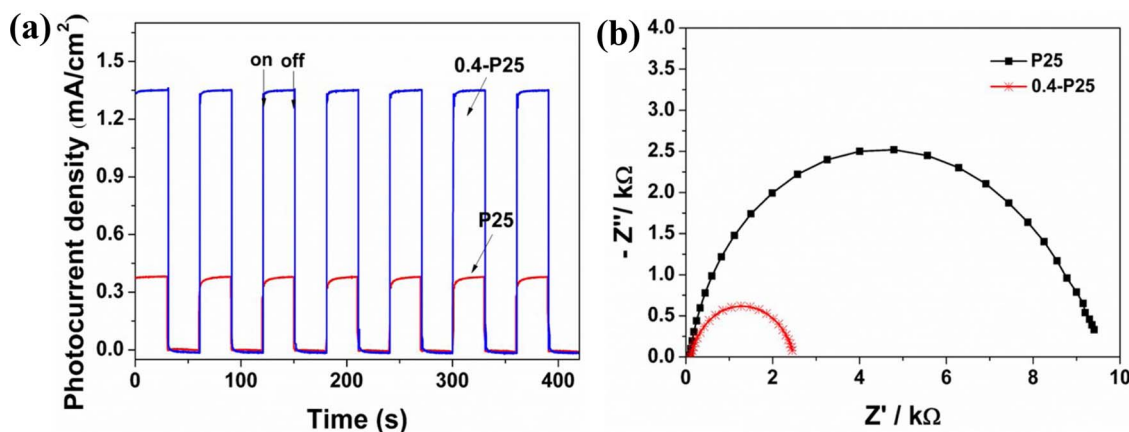


Fig. 5. (a) Transient photocurrent density of P25, and 0.4-P25 electrodes at 0.3 V versus Ag/AgCl; (b) Nyquist plots of electrochemical impedance spectroscopy of the as-prepared samples at -0.4 V vs Ag/AgCl.

mediated by surface defects [45]. The 0.4-P25 achieved a photocurrent higher than $1.25 \text{ mA}/\text{cm}^2$, which is almost four times as high as that of pure TiO_2 , revealing much more effective charge separation and higher activity in CO_2 photocatalytic conversion of the nanocomposite than that of single-component counterpart. Moreover, the charge transfer resistance in dark can be analyzed using EIS. The semicircular Nyquist plot in EIS tests conveys information on charge transfer process with a proportionality between the diameter of the semicircle and the charge transfer resistance. As shown in Fig. 5b, compared with pristine TiO_2 , the semicircle diameter of 0.4-P25 becomes much smaller, reflecting a smaller charge transfer resistance in this heterostructured nanocomposite [46]. In order to study the separated charge carriers directly, P25 and the nanocomposites were selected to conduct time-resolved fluorescence decay spectra (Fig. S5). Deconvolution of these spectra gives average lifetime as listed in Table 1. One can tell that all the nanocomposites' charge carrier average lifetime was prolonged, and that charge carriers existed in 0.4-P25 had the longest lifetime, which is in complete agreement with the above analysis and its highest photocatalytic activity.

3.2. Photocatalytic activity of the samples

The photocatalytic activities of TiO_2 and the nanocomposites were measured by CO_2 photoreduction in a closed gas circulation system operated under ambient pressure with water vapor and high purity CO_2 reactants sealed in the system as previously described [47]. The carbon containing products were quantitative analyzed by gas chromatograph based on the calibration curve and external standard method. Both CO

and CH_4 can be found in the system as shown in Fig. 6, and the production rates were in $\mu\text{mol h}^{-1}$. Control experiments were also carried out as follows: (1) irradiation the reactor without photocatalyst; (2) using pure N_2 instead of high purity CO_2 ; (3) dark experiment without light irradiation. No products in gas phase were found in these control groups, confirming that both the catalysts and light irradiation were essential conditions for the photocatalytic conversion of CO_2 , and that carbonaceous products in other groups came from CO_2 , rather than contaminants in the system. All the tests were performed under simulated solar light irradiation. In addition, compared with nanocomposites in the previous reports, our NCQDs/P25 nanocomposite performed relatively superior photocatalytic activity for CO_2 reduction under Xenon-light irradiation (Table S3).

Fig. 6 shows the accumulated evolutions of main products (CH_4 and CO) as functions of irradiation time over all photocatalysts under light irradiation. It was observed that both CH_4 and CO were much more efficiently generated over nanocomposites than that of P25. To clarify the origin of these carbonaceous products during the photocatalytic reaction, the photoreduction of ^{13}C -labeled CO_2 was carried out under identical photocatalytic reaction conditions (as shown in Fig. S6). The two peaks at $m/z = 29$ and $m/z = 17$ are assigned to ^{13}CO and $^{13}\text{CH}_4$, respectively, indicating that both CO and CH_4 were converted from CO_2 rather than other contaminated carbon. For all the samples studied in this work, the yields of CH_4 and CO on all the photocatalysts are enhanced, while a slight decrease occurred in production rate with prolonged irradiation (Seen in Fig. S7). This decrease in production rate reveals a gradual deactivation of these samples, which has been generally reported in other literature reports, including our previous work

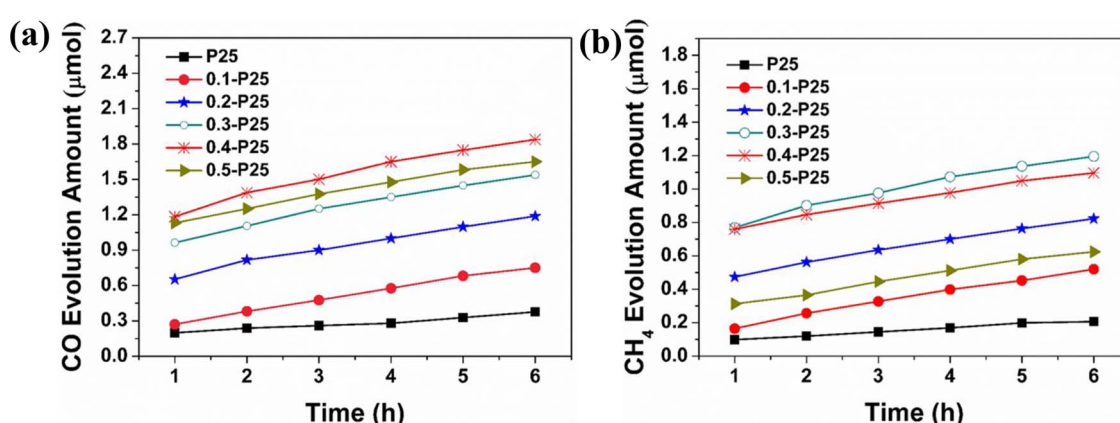


Fig. 6. Time-dependent CO (a) and CH_4 (b) amounts generated on TiO_2 and TiO_2 -based nanocomposites. Condition: 50 mg catalyst, reaction temperature 25 °C, ambient pressure, 300 W Xe-lamp.

[48,49]. The possible reason for this phenomenon might be the relatively slow desorption of products and/or intermediate products from catalysts' activity sites, thus restraining the subsequent steps for CO₂ photoreduction. The heterostructured nanocomposites exhibit much higher photocatalytic activity than TiO₂, suggesting that the decoration with significant synergistic effect [50] is effective in enhancing the photocatalytic activity of TiO₂.

An interesting phenomenon that the products of CO₂ photo-reduction in the presence of water highly depend on catalysts was notable during the evaluation test. For product CO, the photocatalyst 0.4-P25 shows the highest activity, while for CH₄, the sample 0.3-P25 behaves the best among the as-prepared photocatalysts. Nevertheless, the most accumulative amount of carbonaceous products and electron transfer number (n) which was estimated according to Eq. (2) can be obtained over these samples (Fig. S8). Fig. 6 states the accumulated CO and CH₄ amounts from CO₂ photoreduction. It can be seen from Fig. 6a that the yield of CO over TiO₂ is 0.37 μmol after 6 h light irradiation, while the CH₄ amount over TiO₂ is 0.20 μmol as shown in Fig. 6b, which is relatively smaller. Compared with TiO₂, both the evolved CO and CH₄ amounts generated on the nanocomposites are markedly increased, demonstrating that the NCQDs decoration of these nanocomposites played an important role in enhancing the carbonaceous products evolution. The formation of heterostructured junction between NCQDs and TiO₂ promoted the separation and efficient transfer of light induced electrons and holes. Consequently, the prepared nanocomposites exhibited enhanced catalytic performance. However, at a relatively high level of NCQDs addition, the CO and CH₄ yield rates decrease, probably because of shielding effects and formation of new recombination centers for charge carriers in excessive NCQDs species [51].

$$n_e^- = 2 \times n_{CO} + 8 \times n_{CH_4} \quad (2)$$

The typical sample 0.4-P25 was chosen to carry out consecutive photocatalytic reactions. As can be seen in Fig. S9, no deactivation was observed along with prolonged reaction time, demonstrating the good photostability of this photocatalyst. To investigate the materials' structural stability in CO₂ photoreduction with water vapor as reductant, we characterized the structure of the representative nanocomposite 0.4-P25 after photocatalytic tests (seen in Fig. S10). The structure of the used sample showed no obvious change compared with the fresh one, suggesting that the nanocomposite is structurally stable.

3.3. Possible reaction mechanism

Based on the above results, it is known that inducing NCQDs onto TiO₂ have significantly improved the photocatalytic activity of pure TiO₂ under simulated solar light irradiation. Such an enhancement can be mainly attributed to their unique structure with a variety of favorable properties. On the one hand, both rutile and anatase TiO₂ existed in P25 with different band gap and position. Therefore, photo generated charge carriers could transfer efficiently in P25, which would definitely enhance the charge separation. On the other hand, the addition of NCQDs to TiO₂ effectively favors the spectral response ranging from UV to visible light, contributing to the photocatalytic efficiency of these heterostructured nanocomposites in the photoreduction of CO₂ with H₂O [52].

According to band gap theory [53,54] and information described above, a proposal synergistic catalytic mechanism for the CO₂ photoreduction on NCQDs/P25 under simulated solar light irradiation is proposed as illustrated in Fig. 7. Electrons and holes in TiO₂ get separated under full light irradiation. The electrons transfer from the CB band of anatase TiO₂ to that of rutile TiO₂, while the holes transfer on the contrary. The NCQDs play an important role in the enhancement of photocatalytic activity. Firstly, NCQDs can absorb and convert visible light and near-infrared light due to its up-converted property [55]. The converted light with shorter wavelengths could excite TiO₂ to produce charge carriers. Secondly, NCQDs can serve as electron reservoirs to

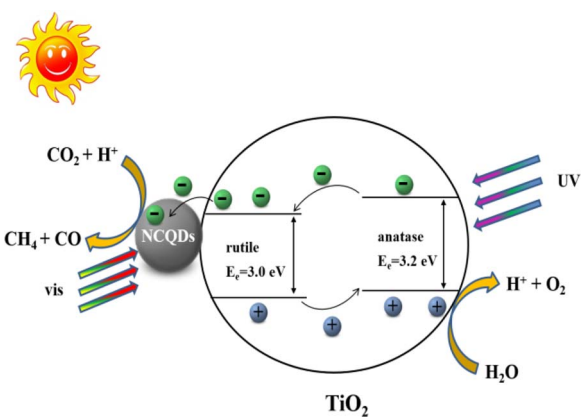


Fig. 7. Schematic illustrations of the proposed mechanism in the NCQDs/TiO₂ heterostructured nanocomposites.

trap photo induced electrons from the conduction band of rutile TiO₂, and thus promote the separation of electron-hole pairs [34], which is proved by photoelectrochemical test as described above. The transient photocurrent response of TiO₂ was significantly increased, while the PL intensity became smaller after introduction of NCQDs to TiO₂, indicating that NCQDs can facilitate the transfer of photogenerated electrons and reduce the recombination rate of electron-hole pairs [52]. At the VB of anatase TiO₂, H₂O molecules are oxidized by h⁺ to generate O₂ and H⁺, meanwhile, at the surface of NCQDs, CO₂ molecules are reduced to CO and CH₄ by accumulated electrons (e⁻) under the assistance of H⁺. The two processes could further prevent the recombination of photogenerated electrons and holes, which resulted in considerably enhanced activity of the photocatalytic reaction.

4. Conclusions

In conclusion, we have demonstrated a series of heterostructured NCQDs/TiO₂ nanocomposites by facile and green microwave assisted method, which exhibit significantly enhanced light response, highly efficient separation and transfer of charge carriers across the interface between the two components, and consequently induce a great enhancement of photocatalytic performance in the photoreduction of CO₂ by gaseous water under stimulated solar irradiation. A possible synergistic catalytic mechanism between NCQDs and TiO₂ is proposed: the NCQDs in the nanocomposites act as photosensitizer to sensitize TiO₂ into visible-light-responsive semiconductor. Furthermore, NCQDs could serve as electrons reservoir. The migration of photo-generated electrons from rutile TiO₂ to NCQDs leads to the recombination prevention of photogenerated electrons and holes, benefiting the activity enhancements of CO₂ reduction. As a result, as high as 1.838 μmol CO and 1.195 μmol CH₄ can be obtained by CO₂ reduction on 50 mg photocatalyst after 6 h irradiation. This work presents a promising NCQDs/TiO₂ photocatalyst for CO₂ photoconversion without addition of any noble-metal co-catalyst.

Acknowledgements

This work was financially supported by the National Natural Science Foundation of China (51702126, 21673102, 21603085), Zhejiang Provincial Natural Science Foundation of China (LQ15B010002), and the Start-up Fund of Jiaxing University (70516036).

Appendix A. Supplementary data

Supplementary material related to this article can be found, in the online version, at doi:<https://doi.org/10.1016/j.apcatb.2018.03.027>.

References

- [1] S. Sato, T. Morikawa, T. Kajino, O. Ishitani, *Angew. Chem. Int. Ed.* 52 (2013) 988–992.
- [2] B. Obama, *Science* (2017), <http://dx.doi.org/10.1126/science.aam6284>.
- [3] X. Zhang, F. Han, B. Shi, S. Farsinezhad, G.P. Dechaine, K. Shankar, *Angew. Chem. Int. Ed.* 51 (2012) 12732–12735.
- [4] T. Inoue, A. Fujishima, S. Konishi, K. Honda, *Nature* 277 (1979) 637–638.
- [5] E. Kondratenko, G. Mül, J. Baltrusaitis, G. Larrazábal, J. Pérez-Ramírez, *Energy Environ. Sci.* 6 (2013) 3112–3135.
- [6] G. Li, Z. Lian, W. Wang, D. Zhang, H. Li, *Nano Energy* 19 (2016) 446–454.
- [7] X. Zhang, Y. Shen, Q. Zhang, L. Gu, Y. Hu, J. Du, Y. Lin, C.-W. Nan, *Adv. Mater.* 27 (2015) 819–824.
- [8] Y. Liu, S. Zhou, J. Li, Y. Wang, G. Jiang, Z. Zhao, B. Liu, X. Gong, A. Duan, J. Liu, Y. Wei, L. Zhang, *Appl. Catal. B: Environ.* 168–169 (2015) 125–131.
- [9] S. Habisreutinger, L. Schmidt-Mende, J. Stolarczyk, *Angew. Chem. Int. Ed.* 52 (2013) 7372–7408.
- [10] Y. Zhang, D. Ma, Y. Zhang, W. Chen, S. Huang, *Nano Energy* 2 (2013) 545–552.
- [11] W. Kim, T. Seok, W. Choi, *Energy Environ. Sci.* 5 (2012) 6066.
- [12] X. Ning, J. Li, B. Yang, W. Zhen, Z. Li, B. Tian, G. Lu, *Appl. Catal. B: Environ.* 212 (2017) 129–139.
- [13] J. Hirayama, Y. Kamiya, *J. Catal.* 348 (2017) 306–313.
- [14] Q. Tay, X. Wang, X. Zhao, J. Hong, Q. Zhang, R. Xu, Z. Chen, *J. Catal.* 342 (2016) 55–62.
- [15] Z. Jin, W. Duan, B. Liu, X. Chen, F. Yang, J. Guo, *Appl. Surf. Sci.* 356 (2015) 707–718.
- [16] S. Obregón, G. Colón, *Appl. Catal. B: Environ.* 144 (2014) 775–782.
- [17] Q. Kang, T. Wang, P. Li, L. Liu, K. Chang, M. Li, J. Ye, *Angew. Chem. Int. Ed.* 54 (2015) 841–845.
- [18] J. Fei, J. Li, *Adv. Mater.* 27 (2015) 314–319.
- [19] T. Wang, X. Meng, G. Liu, K. Chang, P. Li, Q. Kang, L. Liu, M. Li, S. Ouyang, J. Ye, *J. Mater. Chem. A* 3 (2015) 9491–9501.
- [20] C. Han, Y. Wang, Y. Lei, B. Wang, N. Wu, Q. Shi, Q. Li, *Nano Res.* 8 (2014) 1199–1209.
- [21] K. Kondo, N. Murakami, C. Ye, T. Tsubota, T. Ohno, *Appl. Catal. B: Environ.* 142–143 (2013) 362–367.
- [22] Q. Zhang, T. Gao, J. Andino, Y. Li, *Appl. Catal. B: Environ.* 123–124 (2012) 257–264.
- [23] F. Xiao, S. Hung, H. Tao, J. Miao, H. Yang, B. Liu, *Nanoscale* 6 (2014) 14950–14961.
- [24] Y. Chen, W. Huang, D. He, Y. Situ, H. Huang, *ACS Appl. Mater. Interfaces* 6 (2014) 14405–14414.
- [25] Y. Zhu, C. Gao, S. Bai, S. Chen, R. Long, L. Song, Zhengquan Li, Y. Xiong, *Nano Res.* 10 (2017) 3396–3406.
- [26] D. Mosconi, D. Mazzier, S. Silvestrini, A. Privitera, C. Marega, L. Franco, A. Moretto, *ACS Nano* 9 (2015) 4156–4164.
- [27] J. Bian, C. Huang, L. Wang, T. Hung, W.A. Daoud, R. Zhang, *ACS Appl. Mater. Interfaces* 6 (2014) 4883–4890.
- [28] J. Tian, Y. Leng, Z. Zhao, Y. Xia, Y. Sang, P. Hao, J. Zhan, M. Li, H. Liu, *Nano Energy* 11 (2015) 419–427.
- [29] J. Yang, X. Zhou, D. Wu, X. Zhao, Z. Zhou, *Adv. Mater.* 29 (2017) 1604108–1604112.
- [30] Z. Lei, S. Xu, J. Wan, P. Wu, *Nanoscale* 8 (2016) 2219–2226.
- [31] H. Zhang, J.F. Banfield, *J. Phys. Chem. B* 104 (2000) 3481–3487.
- [32] O. Fontelles-Carceller, M. Muñoz-Batista, E. Rodríguez-Castellón, J. Conesa, M. Fernández-García, A. Kubacka, *J. Catal.* 347 (2017) 157–169.
- [33] H. Guo, X. Wang, Q. Qian, F. Wang, X. Xia, *ACS Nano* 3 (2009) 2653–2659.
- [34] N.C.T. Martins, J. Ângelo, A. Girão, T. Trindade, L. Andrade, A. Mendes, *Appl. Catal. B: Environ.* 193 (2016) 67–74.
- [35] X. Lu, G. Wang, T. Zhai, M. Yu, J. Gan, Y. Tong, Y. Li, *Nano Lett.* 12 (2012) 1690–1696.
- [36] N. Lakshmana Reddy, S. Kumar, V. Krishnan, M. Sathish, M.V. Shankar, *J. Catal.* 350 (2017) 226–239.
- [37] M. Li, L. Zhang, X. Fan, M. Wu, M. Wang, R. Cheng, L. Zhang, H. Yao, J. Shi, *Appl. Catal. B: Environ.* 201 (2017) 629–635.
- [38] H. Li, F. Shao, H. Huang, J. Feng, A. Wang, *Sens. Actuators B: Chem.* 226 (2016) 506–511.
- [39] N. Wei, H. Cui, Q. Song, L. Zhang, X. Song, K. Wang, Y. Zhang, J. Li, J. Wen, J. Tian, *Appl. Catal. B: Environ.* 198 (2016) 83–90.
- [40] J. Su, L. Zhu, G. Chen, *Appl. Catal. B: Environ.* 186 (2016) 127–135.
- [41] A. Bourlinos, R. Zboril, J. Petr, A. Bakandritsos, M. Krysmann, E.P. Giannelis, *Chem. Mater.* 24 (2012) 6–8.
- [42] Q. Cui, J. Xu, X. Wang, L. Li, M. Antonietti, M. Shalom, *Angew. Chem. Int. Ed.* 128 (2016) 3736–3740.
- [43] A. Naldoni, M. Allietta, S. Santangelo, M. Marelli, F. Fabbri, S. Cappelli, C.L. Bianchi, R. Psaro, V.D. Santo, J. Am. Chem. Soc. 134 (2012) 7600–7603.
- [44] B. Zielinska, J. Grzehulska, B. Grzmil, A.W. Morawski, *Appl. Catal. B: Environ.* 35 (2001) 127–135.
- [45] D. Jiang, W. Wang, S. Sun, L. Zhang, Y. Zheng, *ACS Catal.* 5 (2015) 613–621.
- [46] J. Song, H. Ryoo, M. Cho, J. Kim, J. Kim, S. Chung, J. Oh, *Adv. Energy Mater.* 3 (2017) 1601103–1601110.
- [47] M. Li, L. Zhang, M. Wu, Y. Du, X. Fan, M. Wang, L. Zhang, Q. Kong, J. Shi, *Nano Energy* 19 (2016) 145–155.
- [48] Z. Sun, Z. Yang, H. Liu, H. Wang, Z. Wu, *Appl. Surf. Sci.* 315 (2014) 360–367.
- [49] M. Li, L. Zhang, X. Fan, Y. Zhou, M. Wu, J. Shi, J. Mater. Chem. A 3 (2015) 5189–5196.
- [50] J. Shi, *Chem. Rev.* 113 (2013) 2139–2181.
- [51] K. Chang, Z. Mei, T. Wang, Q. Kang, S. Ouyang, J. Ye, *ACS Nano* 8 (2014) 7078–7087.
- [52] X. Yu, J. Liu, Y. Yu, S. Zuo, B. Li, *Carbon* 68 (2014) 718–724.
- [53] H. Xu, J. Yan, X. She, L. Xu, J. Xia, Y. Xu, Y. Song, L. Huang, H. Li, *Nanoscale* 6 (2014) 1406–1415.
- [54] S. Kumar, M. Isaacs, R. Trofimovaitė, L. Durndell, C. Parlett, R. Douthwaite, B. Coulson, M. Cockett, K. Wilson, A. Lee, *Appl. Catal. B: Environ.* 209 (2017) 394–404.
- [55] H. Yu, Y. Zhao, C. Zhou, L. Shang, Y. Peng, Y. Cao, L.-Z. Wu, C.-H. Tung, T. Zhang, J. Mater. Chem. A 2 (2014) 3344.